

Main Drying and Wetting Curves of Soils: On Measurements, Prediction and Influence on Wave Propagation

Bettina ALBERS

*Technical University of Berlin, Institute for Geotechnical
Engineering and Soil Mechanics*

Germany

e-mail: albers@grundbau.tu-berlin.de

Depending on the initial degree of saturation of a soil, different capillary pressure curves occur. If a sample is initially water saturated and then drained (process of drainage) the main drying curve results. On the other hand, if the sample is initially dry and water is supplied until saturation is reached (process of imbibition) the main wetting curve is the consequence. These two curves build a hysteresis loop. If after the first process the other is followed up (possibly a number of times), then inner hysteresis curves arise. The focus of this paper is the investigation of some aspects of the main drying curve (MDC) and the main wetting curve (MWC). Some methods of their measurement are discussed. Because of big differences in the capillary pressure for different degrees of saturation the measurement is laborious and time consuming and often application of more than one method is necessary. Consequently, often only the MDC is measured and the data is used to predict the MWC and inner curves. Exemplarily, one prediction method is shown and subsequently, for one soil type the resulting curves are used to calculate the wave speeds and attenuations of the appearing sound waves. The dependence of these wave features on frequency and saturation for the current example shows, that the hysteresis effect of the capillary pressure curve has only a slight effect on the propagation of sound waves in partially saturated sand.

Key words: capillary pressure curves, partially saturated porous media, hysteresis.

1. INTRODUCTION

The final aim of the investigation of certain aspects of partially saturated soils is the preferably closed-form description of the propagation of sound waves including the hysteresis effects of the capillary pressure curve. Partially saturated soils consist of three components: the solid (index S) and two immiscible pore fluids (indices F and G) which here are expected to be water and air.

Although it is well known that the capillary pressure exhibits two branches depending on the initial state of the sample, for simplicity in earlier investigations (e.g. [6]) only one of them has been considered. In order to describe wave propagation processes a hyperbolic model is needed. Such a model has been introduced in [7] and applied to the wave propagation in air-water mixtures in sandstones [4] and other soil types [5, 8]. The wave propagation analysis predicts the existence of four sound waves in partially saturated porous media – one transversal wave, S , and three compressional waves, $P1$, $P2$ and $P3$. Their phase speeds and attenuations are determined in dependence on frequency and degree of saturation, i.e. of the fraction of the wetting pore fluid to the whole void volume. The $P1$ -wave is mainly driven by the skeleton. The $P2$ -wave shows a similar behavior to the sound wave in suspensions: its speed has a deep minimum in dependence on the saturation. The $P3$ -wave only exists if at least two immiscible pore fluids occur (in the case of one fluid filling the pores, the soil is called 'saturated'). Its speed is attributed to the capillary pressure between the pore fluids. This enters the model by the use of an empirical law by van Genuchten [42]

$$(1.1) \quad p_c = \frac{1}{\alpha_{vG}} \left[S_e^{(-1/m_{vG})} - 1 \right]^{1/n_{vG}} .$$

This relation, which obviously only describes one of the branches of the capillary pressure curve (see the left panel of Fig. 1), contains three parameters m_{vG} , n_{vG} and α_{vG} . The choice of these parameters controls the shape of the curve (m_{vG} and n_{vG}) and its position in the capillary pressure-saturation-diagram (α_{vG}). The effective saturation S_e accounts for the fact that for most soil types in the limits of the capillary pressure there remains a certain amount of the other pore fluid – the residual saturation or irreducible saturation – in the pores.

As mentioned above, with the van Genuchten formula usually only the main drying curve is described. However, depending on the initial degree of saturation of a soil, different capillary pressure curves occur. If a sample is initially water saturated and then drained (process of drainage; see left hand side of Fig. 2) the main drying curve (MDC) results. On the other hand, if the sample is initially dry and water is supplied until saturation is reached (process of imbibition; see right hand side of Fig. 2) the main wetting curve is obtained. These two curves, often also called boundary curves, build a hysteresis loop (see right panel of Fig. 1). This figure also demonstrates that, if after the first drying or wetting process the opposite process follows subsequently, then primary curves arise. Further cycles of wetting or drying lead to further inner – so called – scanning curves.

Figure 2, showing the capillary menisci during drainage and imbibition of a soil sample, impressively illustrates the effect of surface tension. The surface of

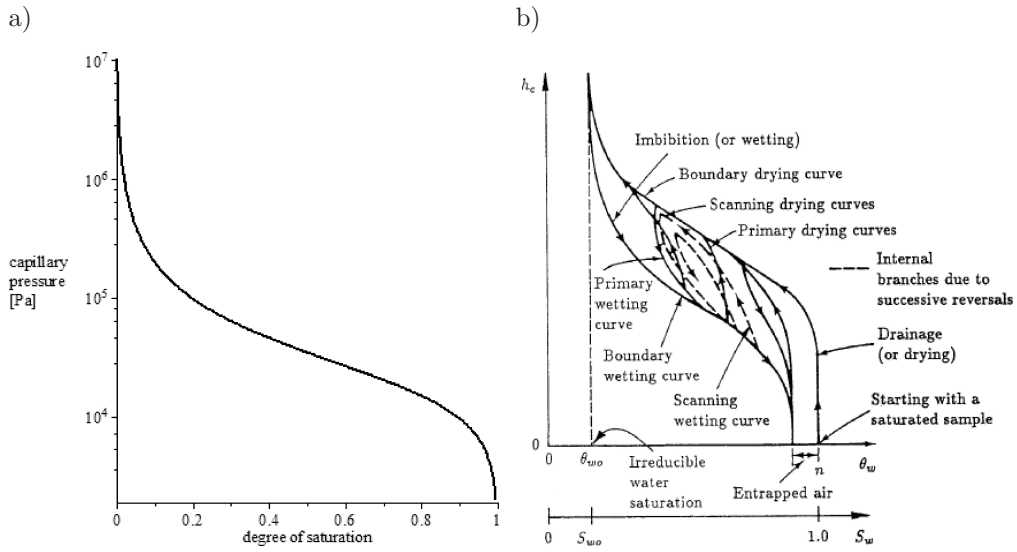


FIG. 1. a) Main drying curve for sandstone created with the van Genuchten formula (1.1); b) hysteresis in capillary pressure curves, main (boundary) wetting and drying curves and inner (scanning) curves (taken from BEAR and BACHMAT [11]).

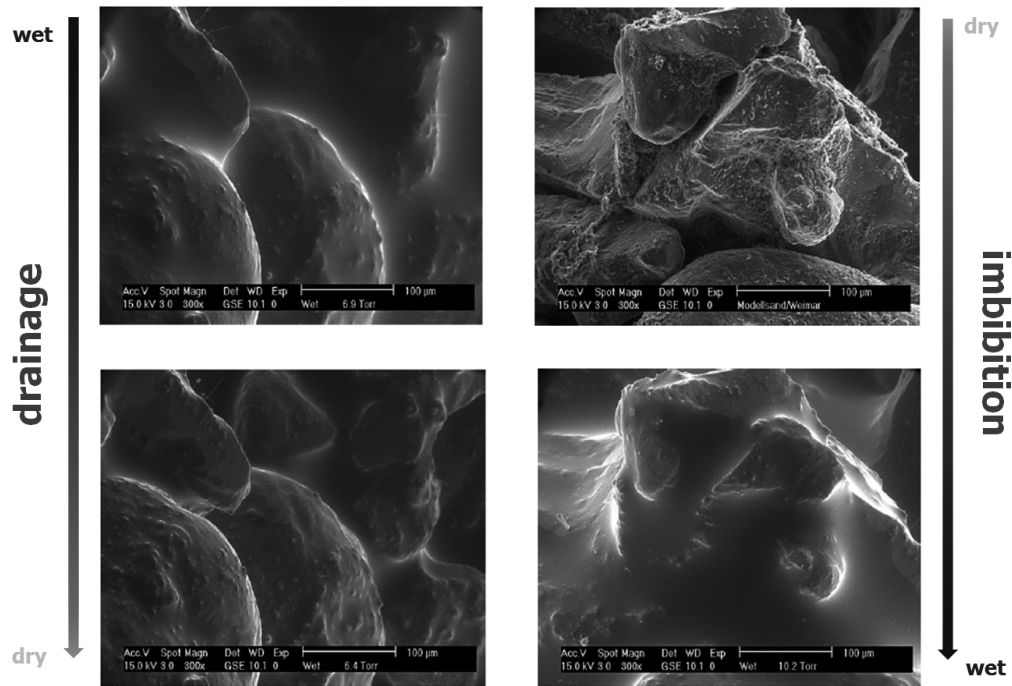
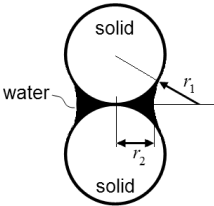


FIG. 2. Capillary menisci during drainage (left) and imbibition (right); figures from [38].

soil particles is curved and has two principal radii of curvature, r_1 and r_2 (see the following figure which is based on a figure of a pendular ring of REINSON, FREDLUND & WILSON [37]). They are the radii of a water-air interface. By considering the change in the direction of the forces acting on opposite sides, one obtains the Young-Laplace equation

(1.2)



$$\Delta p = p_c = p_2 - p_1 = \sigma_{12} \left(\frac{1}{r_1} + \frac{1}{r_2} \right) = 2 \frac{\sigma_{12}}{r^*},$$

where r^* is the mean radius of curvature ($2/r^* = 1/r_1 + 1/r_2$). The capillary pressure is, thus, a measure of the tendency of a porous medium to suck in the wetting fluid (whose molecules or atoms are preferentially adsorbed on solid surfaces) or to repel the nonwetting phase. The radius r^* is of the order of magnitude of the pore or grain size. The capillary pressure, thus, depends on the geometry of the void space, on the nature of the solids and fluids and on the degree of saturation. In soils, the geometry of the void space is extremely irregular and complex. Hence, the determination of radii r_1 and r_2 is nearly impossible and instead an idealized model may be adopted. Laboratory experiments are probably the only method to derive the relationship $p_c = p_c(S)$.

The phenomenon of hysteresis, i.e. different values of the capillary pressure for the same degree of saturation for drying and wetting, is attributed to a number of causes. The first, called ink-bottle effect, results from the shape of the pore space with interchanging narrow and wide passages (for an illustration see Fig. 3, top left). During drainage and re-wetting, menisci having the same curvature occur at different elevations, thus yielding different wetting fluid saturations for the same capillary pressure. The second, called the raindrop effect (see Fig. 3, top right), is due to the fact that the contact angle at the advancing trace of an interface on a solid differs from that at the receding one. This happens, e.g. because of impurities, roughness or variability of the solid surface. The third cause for hysteresis is the entrapment of droplets in the void space as the non-wetting fluid is replaced by the wetting one during wetting the sample. This effect is called snap-off and it is illustrated in the bottom of Fig. 3. It occurs if the void space diameter is very different from the void opening diameter. Of course, also the non-wetting fluid can be entrapped in the pore space during re-wetting. Finally, especially in fine porous media, consolidation, swelling and shrinkage of the solid matrix may contribute to hysteresis in the capillary pressure curve.

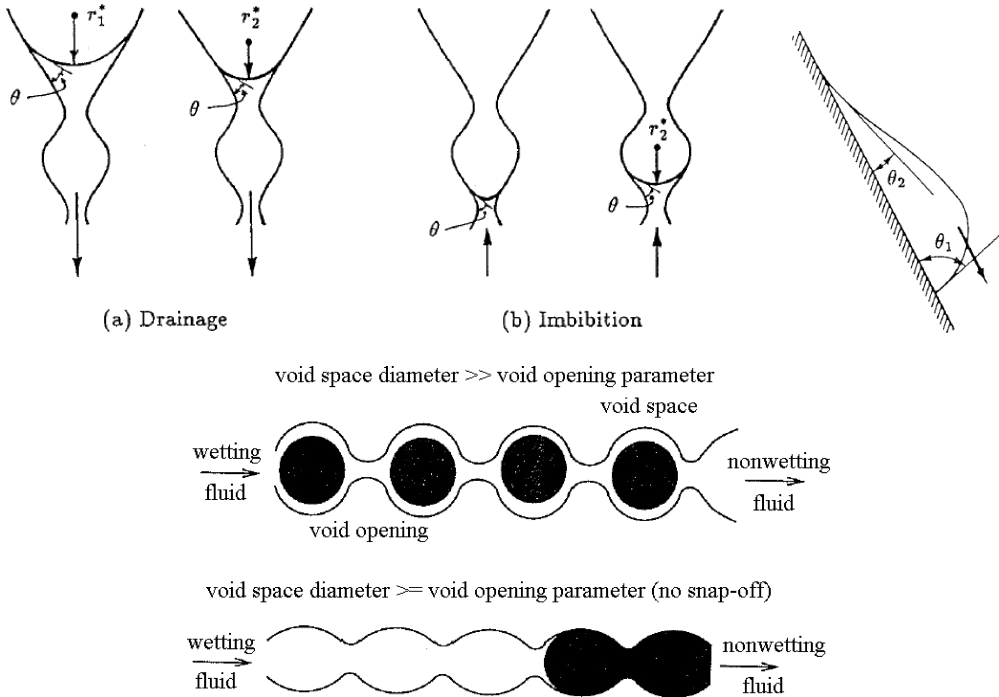


FIG. 3. Illustration of causes for hysteresis in capillary pressure curves. Top left: ink-bottle effect, top right: raindrop effect (both taken from BEAR and BACHMAT [11]), bottom: snap-off effect (taken from SHETA [40]).

2. MEASUREMENTS

The relation between the water content and the matric potential in a soil is referred to by various names, such as water retention curve, soil water characteristic curve (SWCC), water content-matric potential curve or capillary pressure-saturation relation. This function relates a capacity factor, the water content, to an intensity factor, the energy state of the soil water. The energy state is expressed by names such as suction, tension, capillary pressure (head) or matric head. The potential of the soil water may be expressed in units of energy per unit mass [J kg^{-1}], energy per unit volume [Pa] or energy per unit weight [m]. The latter corresponds to the matric head which is expressed as the height of a fluid column of a given density. While suction, tension and capillary pressure values are positive, the matric head is negative. The soil water content may be expressed on a weight basis (gravimetric water content [kg kg^{-1}]), on a volume basis (volumetric water content [$\text{m}^3 \text{m}^{-3}$]) or on a degree of saturation basis (ratio of volumetric water content and volumetric pore content). The water retention relation is hysteretic which means that the water content/saturation

during drainage will be greater than during wetting for a given value of the matric head/capillary pressure [16].

The probably first measurements of such curves for different types of soils were conducted by E. BUCKINGHAM [13] in 1907. He obtained curves from columns of six soils of various types, analyzed after from fifty-three to sixty-eight days, when they had apparently ceased to take up any more water. The soils were in metal cylinders 48 inches long and 2.5 inches in diameter, closed at the top. Water was supplied through side tubes at the bottom. He plotted the height from the water level over the water content in percent (see Fig. 4). It is obvious that he only measured one of the branches of the water retention curve.

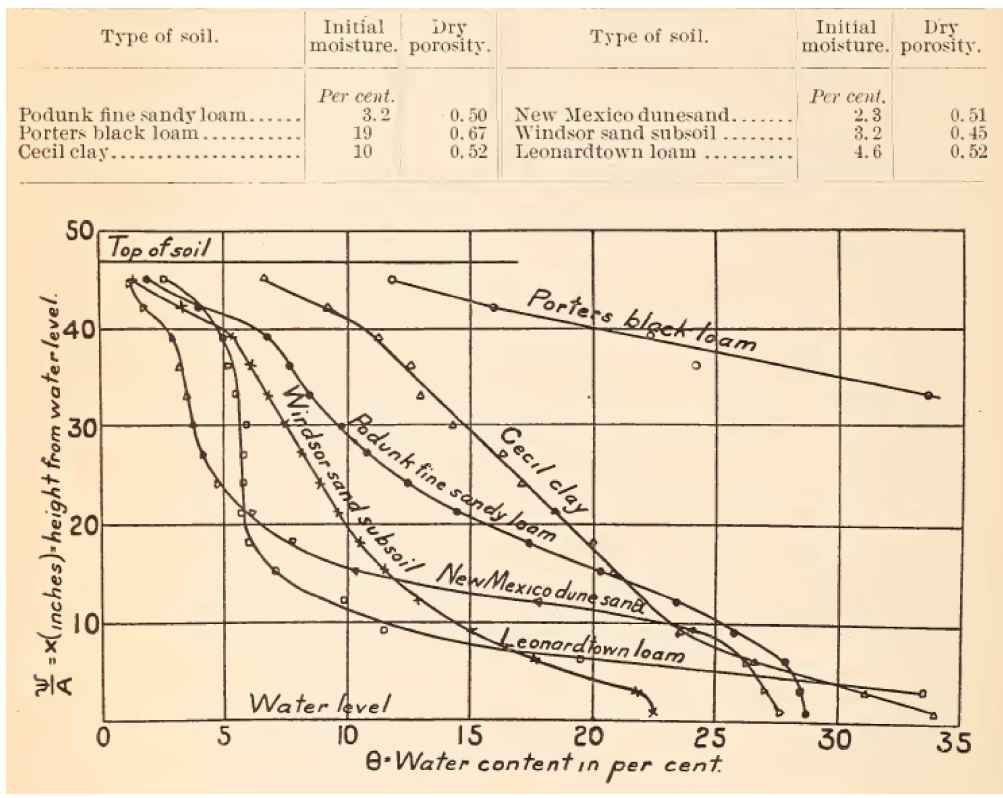


FIG. 4. Distribution of water in 48-inch columns of soil after 53 to 68 days (from BUCKINGHAM [13] 1907).

In the following description of different contemporary measuring methods for water retention curves, we mainly rely on the book by LU and LIKOS [29]. Therein the term total suction quantifies the thermodynamic potential of soil

pore water relative to a reference potential of free water. Free water has no interactions with other components which impart curvature to the air-water interface and has no external forces other than gravity. Total suction is considered as the sum of matric suction and osmotic suction. The former arises from the combined effects of capillarity and short-range adsorption. The term “matric” stems from the term “matrix” since it stands for the part of suction arising from interaction between the pore water and the soil solid or soil matrix. Osmotic suction arises from the presence of dissolved solutes. While short-range adsorption and osmotic effects may also appear in saturated soils capillarity effects are unique to unsaturated or partially saturated soils.

As pointed out above, the range of suction is very large. This is especially true for soils with very fine grains because the capillary forces arising in the small voids are exceptionally high. For such soil types one measuring method may not be sufficient to determine the whole curve. LU and LIKOS [29] divide the measuring techniques in such a way to find the matric suction (methods a)–d) in Fig. 5) and others for the determination of total suction (methods e)–h) in Fig. 5). Although the first group seems to be more important also the second group will be presented roughly. In the figure the ranges of the different measuring methods are compared to the Soil Water Characteristic Curves (SWCC) of three soil types. Note that in the upper part of the figure the suction is given in kPa while in the bottom part in MPa.

Both methods a) by tensiometers and b) axis translation techniques rely on the properties of so-called High-Air-Entry materials (HAE). On the right hand side of the following figure the reproduction from [29] of a sketch of the situation is presented. Saturated HAE materials have the capability of restricting the advection of air while allowing free advection of water. If a soil sample is placed in contact with a saturated HAE material, air pressure which acts on the air in the pores may be applied on one side and the pore water may freely drain through the material under atmospheric pressure maintained on the other side. The separation of air and water pressure happens as long as the applied pressure does not exceed the air-entry pressure of the HAE material. The air-entry pressure of a certain material is reflected by the beginning of the deviation from the horizontal part (for low suction values) of the curves (see Fig. 5, bottom). It is determined by the radius of the largest pore. The smaller the largest pore, the higher the air entry value.

a) Tensiometers (suction range 0–100 kPa)

The surface tension acts as a membrane for separating the two phases, thus, allowing the negative water pressure to be directly measured. Pore pressure measurements are made by a direct exchange of water between the sensor and the soil. Negative pressure is transmitted through the saturated pores of the HAE ceramic tip such that water is withdrawn from the

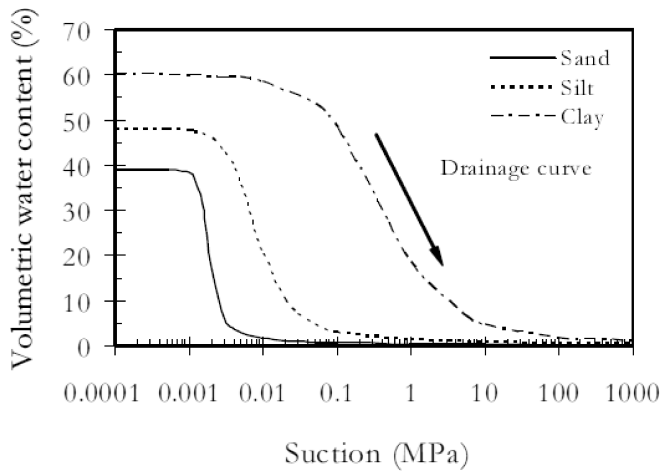
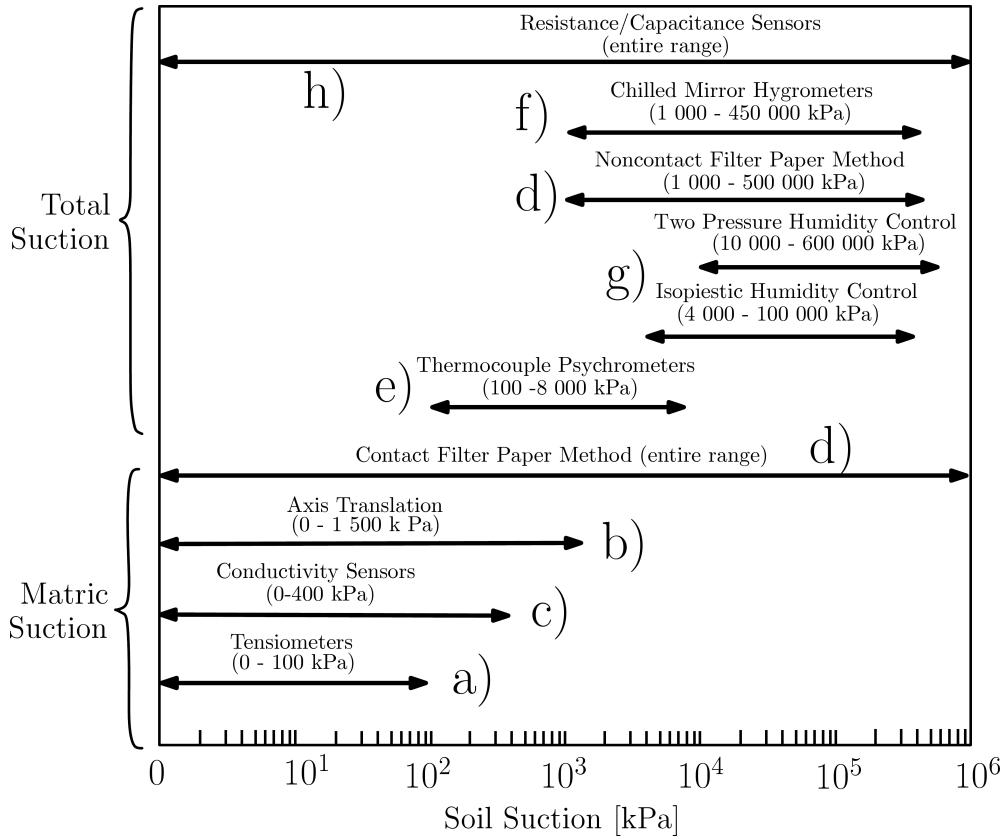
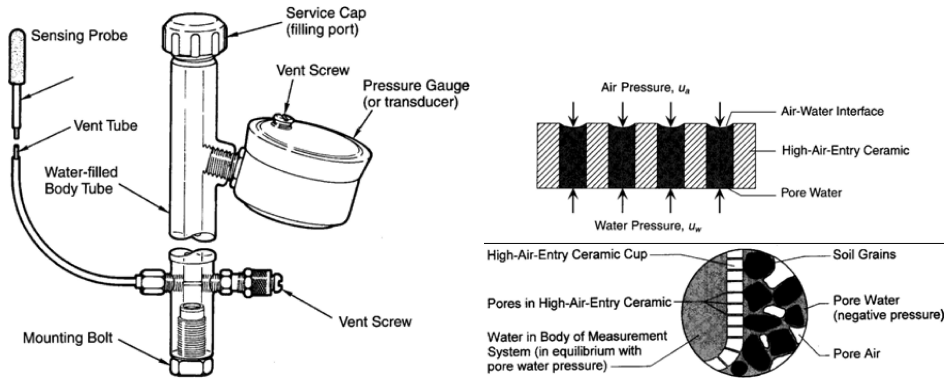


FIG. 5. Top: Ranges of several soil suction measuring methods (after [29]), bottom: qualitative view of the Soil Water Characteristic Curves (SWCC) of three soil types – compare the ranges to the measuring methods in the upper panel of the figure considering that there the suction is given in [kPa] here in [MPa] (from [28]).

tensiometer until the internal pressure in the sensor body is equivalent to the matric potential of the soil water.

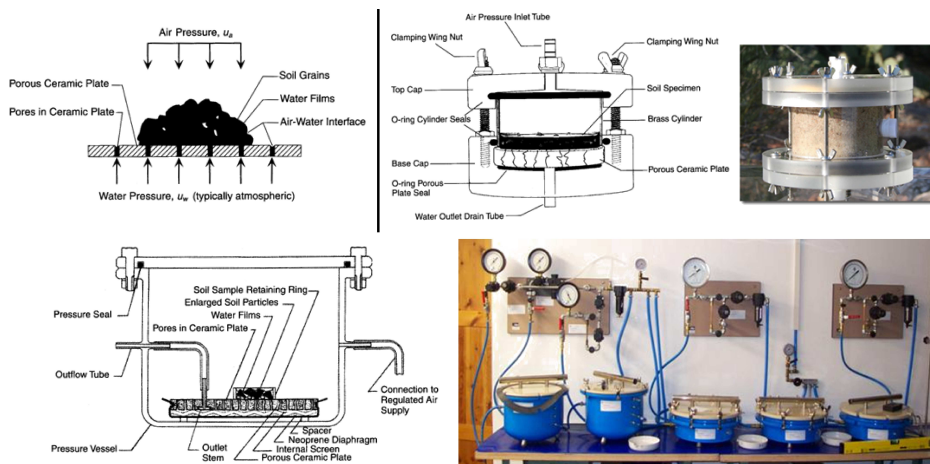
Left: Schematic drawing of a tensiometer, top right: operating principle of an HAE ceramic disk showing how air and water pressure are separated by surface tension, bottom right: schematic showing a porous ceramic tip in contact with unsaturated soil grains (figures from [29]).



b) Axis translation

Axis translation techniques rely on controlling the difference between the pore air pressure and pore water pressure and measuring the corresponding water content of soil in equilibrium with the applied matric suction.

Top left: Schematic drawing of the interface between unsaturated soil and a HAE disk for an axis translation measurement, top right: Tempe cell, bottom: pressure plate (drawings from [29], picture of the Tempe cell [3], picture of the pressure plates [2]).



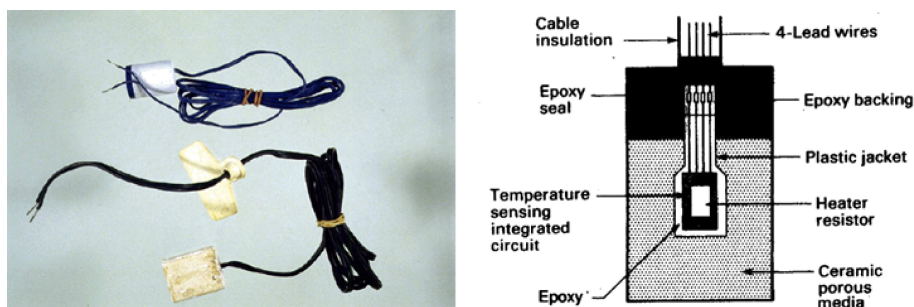
Pressure plates (suction range 0–1 500 kPa) consist of a steel vessel and a saturated HAE ceramic plate. The latter are designated by different air-entry pressures. A small water reservoir is formed beneath the plate and is vented to the atmosphere through an outflow tube allowing the air pressure in the vessel and the water pressure in the reservoir to be separated. Soil samples are initially saturated. The air pressure in the vessel is then increased and simultaneously, the pore water is allowed to drain. The outflow of the water content is monitored until it ceases.

Tempe cells (suction range 0–100 kPa) are similar in concept. However, while in pressure plates several soil samples can be investigated simultaneously, in Tempe cells points of the soil characteristic curve of only a single sample are measured. They are smaller than pressure plates.

c) Conductivity sensors (electrical/thermal, suction range 0–400 kPa)

The electrical and thermal conductivities of a rigid porous medium (a ceramic block) are direct functions of the water content. If such a porous medium is embedded in a mass of unsaturated soil, any change in the suction of the soil results in a corresponding change in the water content of the porous medium. Sensors measuring the change of water content are typically constructed of porous ceramic, polymer synthetics, sintered metal/glass, or gypsum plaster – their notion used in practice is gypsum blocks. The thermal conductivity is measured by measuring the rate of internal heat dissipation following an applied heat pulse, the electrical conductivity by use of two embedded electrodes. However, the latter measurements are difficult because of the inherent sensitivity to changes in electrical conductivity which are not related to the moisture content, e.g. from dissolved solutes.

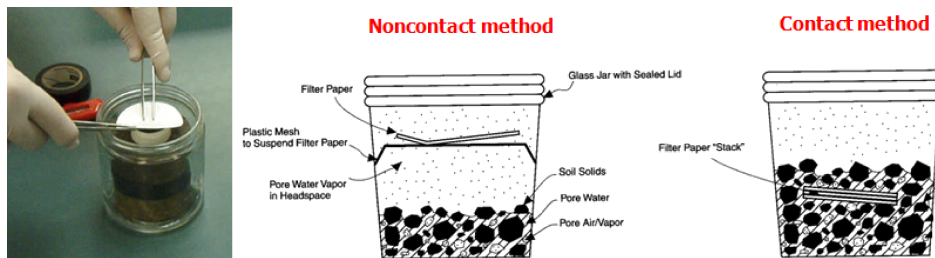
Left: picture of two types of gypsum blocks (from [15]), right: cross-sectional diagram of a thermal conductivity sensor (from [20]).



d) Filter paper method (contact and noncontact)

Both the contact and noncontact filter paper techniques estimate soil suction indirectly by measuring the amount of moisture transferred from an unsaturated soil specimen to an initially dry filter paper. They are relatively simple, low-cost and reasonably accurate alternatives to other methods. In both cases (measurement of matric suction by the contact method (suction range: 0–10⁶ kPa) and of total suction by the noncontact method (suction range: 1 000–500 000 kPa) the moisture content of the filter paper at equilibrium is measured gravimetrically and related to soil suction through predetermined calibration curves. Calibration curves for drying and wetting are given for different types of filter papers by the producer (for an example see [14]). For the noncontact method a filter paper is suspended in the headspace above the sample so that moisture transfer occurs in the vapor phase. For the contact method the papers are placed in direct contact with the sample so that the moisture transport is controlled by capillary and particle surface adsorption forces.

Left: Demonstration of the noncontact filter paper method (from [14]), right: general testing configurations for filter paper testing: noncontact method for total suction measurement, contact method for matric suction measurement (drawings from [29]).

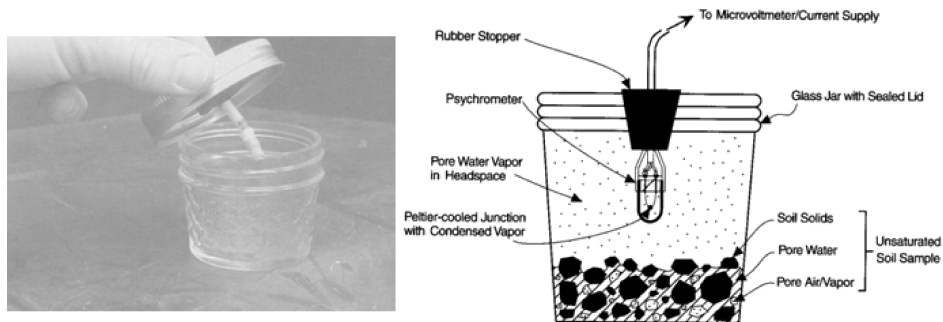


e) Thermocouple psychrometers

Psychrometers operate on the basis of temperature difference measurements between a nonevaporating (i.e. dry) surface and an evaporating surface (i.e. wet bulb). Thermocouple psychrometers (suction range: 100–8 000 kPa) contain an electrical circuit formed by thin wires of dissimilar metals housed within a shield of porous ceramic or stainless steel mesh. The Peltier effect, namely the cooling or warming of the junctions by passing an electrical current through the circuit, is used: Depending on the direction of the applied current the junctions either adsorb or liberate heat in an amount that is a function of the magnitude of the current.

If the temperature of the cooling junction is depressed beyond the dew-point temperature of the ambient environment, then water condenses on the junction at a temperature that is a function of the ambient relative humidity [29].

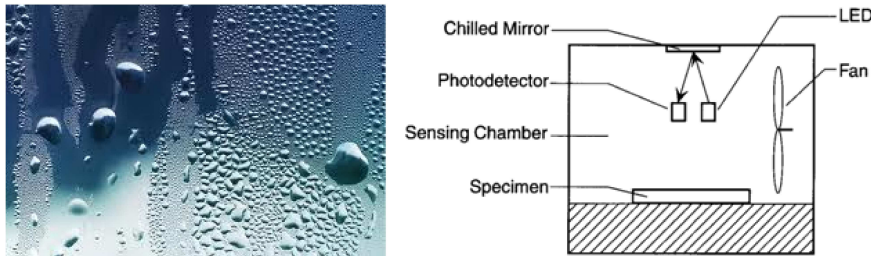
Photograph and schematic drawing of a typical laboratory set up for measuring total suction using a thermocouple psychrometer (both from [29]).



f) Chilled mirror hygrometers (suction range: 1–450 MPa)

Humidity measurement involves thermoelectric chilling of a reflective surface, usually a metallic mirror, to a temperature at which condensation of ambient water vapor is visible on the mirror surface.

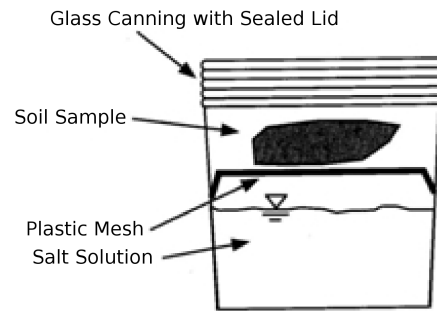
Left: condensation at a window glass (from [1]), right: schematic diagram of the chilled-mirror sensing technology (from [29]).



g) Isopiestic humidity control (suction range: 4–600 MPa)

Using isopiestic humidity control, saturated or unsaturated salt or acid solutions are allowed to come to the thermodynamic equilibrium in small sealed containers. Under isothermal conditions the relative humidity in the headspace above the solution approaches a fixed, reproducible value which is dependent on the solution concentration.

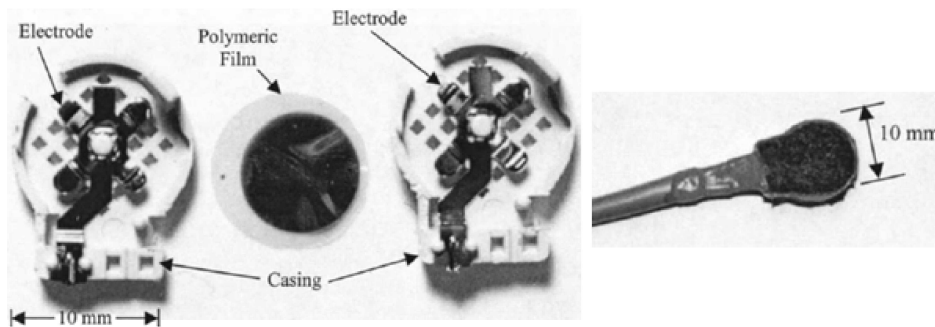
Example testing configuration using isopiestic humidity control (from [29]).



h) Humidity/capacitance sensors

In semiarid and arid regions soils can be so dry that total suctions and soil gas relative humidities may exist at values beyond the limits for which thermocouple psychrometers can be used (8 MPa or 94%). Polymer sensors (see the subsequent figure) consist of two electrodes separated by a film of thermoset polymer that absorbs or releases water as the relative humidity of the surrounding gas changes. Measurements of resistance or capacitance of the polymer film are used along with a calibration curve to determine the relative humidity. The electrodes and polymer film are enclosed in a porous body.

Polymer capacitance sensor: components and sensor assembled with lead wire, sealant, and geotextile covering (from [10]).



3. PREDICTION

3.1. One branch

As mentioned in Sec. 2 different authors use different quantities to describe the water retention, or rather the capillary pressure curve. For instance, in [21]

the soil water retention curve $h(\theta)$ relates the soil water pressure head h [L] to the volumetric soil water content θ [L^3/L^3], while e.g. in [6] the in continuum mechanics commonly used equivalent description of the capillary pressure curve $p_c(S)$ relating the capillary pressure p_c [Pa] to the degree of saturation S [-] is used. In both cases a full description of the relationship requires three parameters: one shape parameter and a scale parameter for each of the two variables. Such a description e.g. was introduced by van GENUCHTEN in 1980 [42]. He related the dimensionless water content Θ to the pressure head by the equation

$$(3.1) \quad \Theta = \left[\frac{1}{1 + (\alpha h)^n} \right]^m, \quad \Theta = \frac{\theta - \theta_r}{\theta_S - \theta_r},$$

where α , n and m are the above mentioned three – as yet undetermined – parameters, indices S and r indicate saturated and residual values of the water content θ and the pressure head h is assumed to be positive. The equivalent in the other type of representation is (compare (1.1))

$$(3.2) \quad S_e = \left[\frac{1}{1 + (\alpha_{vG} p_c)^{n_{vG}}} \right]^{m_{vG}}, \quad S_e = \frac{S - S_r}{1 - S_r},$$

in which S_e denotes the above mentioned effective saturation accounting for the residual (irreducible) fluid saturation S_r (compare Fig. 1 (right)). While $m \equiv m_{vG}$ and $n \equiv n_{vG}$, α_{vG} is different from α because of unequal units of h and p_c . Relation (3.1) does not account for the hysteresis, i.e. the fact that the water content at a given pressure head is higher during drying than during wetting. In his work [42] van Genuchten fits the parameters to experimental data but he does not point out which of the two branches is described. Van Genuchten mentioned that after the Mualem conductivity model [31] the number of parameters can be further limited by the relation

$$(3.3) \quad m = 1 - \frac{1}{n} \quad \text{for } n > 1.$$

Sometimes the water content is related to the matric potential ψ [Pa] rather than to the pressure head. This is done e.g. in the German standard DIN 4220 [17] in which 31 soil types are classified. Amongst other soil properties, statistically determined results and van Genuchten parameters for a *medium* soil-water characteristic curve (average between main drainage and main imbibition curve?) are given (they are illustrated in Fig. 6). After transformation of these values (left panel of the figure) into the form (3.2) the wave speeds and attenuations of the four types of acoustic waves appearing in partially unsaturated soils have been calculated in [6] for twelve soil types. In order to investigate the influence of the hysteresis on the wave propagation measurements of the MDC and MWC of these soil types have been ordered in a soil lab. Once available they will serve to identify the range of possible speeds and attenuations of the waves.

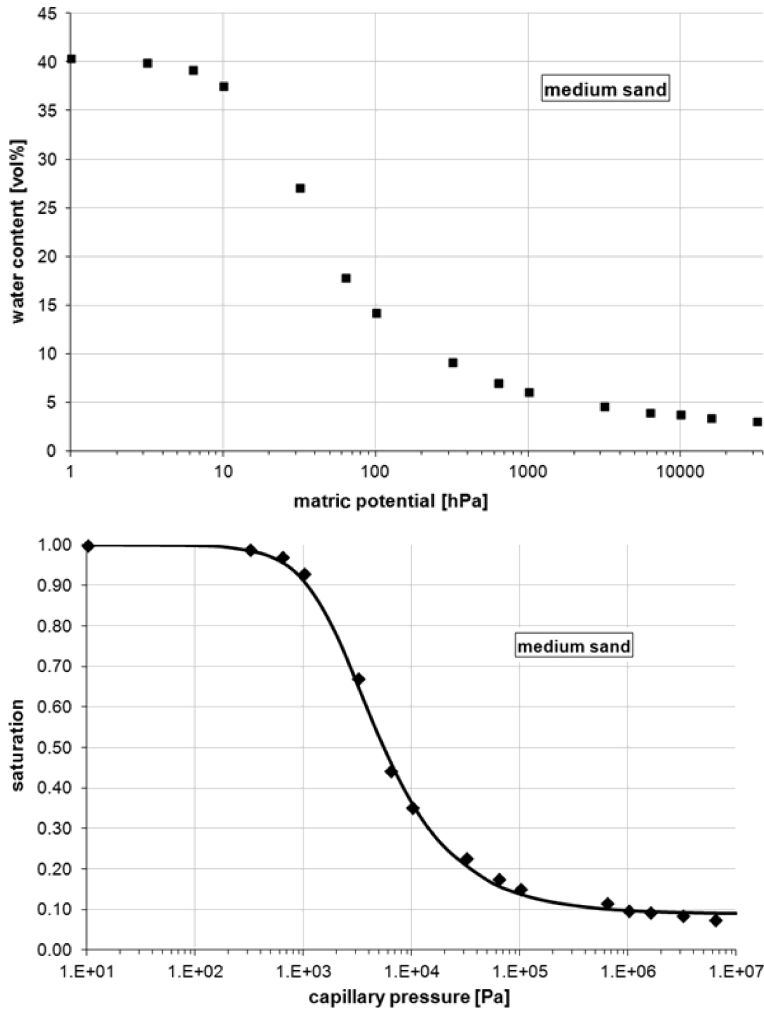


FIG. 6. Top: statistically determined values for the matric potential in dependence on the water content for medium sand (values taken from [17]), bottom: values from the left panel rescaled to a capillary pressure-saturation dependence and van Genuchten curve resulting from (3.2).

3.2. Main curves

Most hysteresis models for soils presented in the literature (on modeling hysteresis see e.g. [9]) presume that both MDC and MWC are measured and interpolate scanning curves (i.e. inner curves for further drying and wetting processes) from the data of both curves. The majority of models is based on the independent domain theory which goes back to works of NEEL [32], EVERETT [19], ENDERBY [18] and POULOVASSILIS [36]. Only the latter approach

focused on soil-moisture hysteresis and was the basis for a couple of theories to interpolate scanning water retention curves from both main drying and wetting curves (e.g. TOPP [41] or MUALEM [30]). Also some further empirical hysteresis models rely on values of both main curves, i.e. for instance, SCOTT *et al.* [39], KOOL and PARKER [25] or PARKER and LENHARD [33]. PARLANGE [34] presented in 1976 an approach to predict the second boundary and scanning curves in between from only one boundary curve. Since the measurements – as we have seen in the last section – are laborious and time consuming this offers advantages compared with other methods. The basic equation of the original model [34], is

$$(3.4) \quad \theta_d(h, h_{std}) = \theta_w(h) - [h - h_{std}] \frac{d\theta_w}{dh}, \quad \theta_d \leq \theta_{std} = \theta(h_{std}),$$

in which the subscripts *d* and *w* refer to drying and wetting, estimates a primary drying curve starting at a given soil water pressure head h_{std} on the wetting curve (for clarification see Fig. 7). Integration of (3.4) gives an equation for the primary wetting curve starting at a pressure head $h_{stw}(\theta_{stw})$ on the drying curve. An inconvenience of this model is that it imposes a wetting curve without an inflection point (see Fig. 7 left) [21]. For the original model no analytical solution applied to the van Genuchten equation could be found. However, for

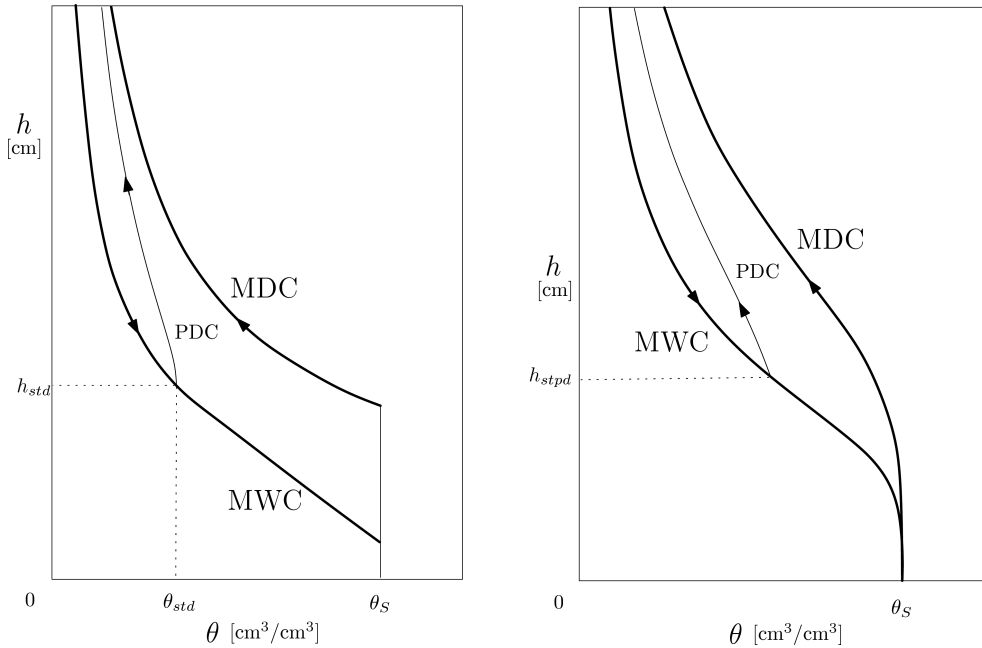


FIG. 7. Left: Schematic diagram of the PARLANGE hysteresis model [34] with the main wetting curve MWC, the main drying curve MDC and a primary drying curve PDC with starting point; right: Schematic diagram of the HAVERKAMP *et al.* hysteresis model [21] with the main wetting curve MWC, the main drying curve MDC and the primary drying curve PDC.

the construction of the model presented in [6] which will be used to compare results with and without hysteresis this approach has been used. Therefore, an extension by HAVERKAMP *et al.* [21] is introduced here which implies that all drying and wetting curves (regardless of the scanning order) have the shape of the van Genuchten Eq. (3.1) in normalized form

$$(3.5) \quad \theta^* = \frac{\theta - \theta_r}{\theta_S - \theta_r} = \left[1 + \left(\frac{h}{h_g} \right)^n \right]^{-m},$$

where the soil pressure head h [L] is taken to be negative and h_g denotes the van Genuchten pressure head scale parameter. HAVERKAMP *et al.* state that for large negative pressure heads only the product mn is significant. They point out that for the majority of soils $0 < mn < 1$ and call the product the water retention shape indicator.

The above mentioned postulation that all curves are expressed in form of the van Genuchten function leads to the following equations for the MWC and the MDC

$$(3.6) \quad \begin{aligned} \theta_{mw}^* &\equiv \frac{\theta_{mw}}{\theta_{Smw}} = \left[1 + \left(\frac{h}{h_{gmw}} \right)^{n_{mw}} \right]^{-m_{mw}}, \\ \theta_{md}^* &\equiv \frac{\theta_{md}}{\theta_{Smd}} = \left[1 + \left(\frac{h}{h_{gmd}} \right)^{n_{md}} \right]^{-m_{md}}, \end{aligned}$$

where the subscripts mw and md refer to main wetting and main drying, respectively. Differently from the Parlange model these curves possess an inflection point (see Fig. 7 right) and the two main points meet at $\theta_{Smw} = \theta_{Smd} = \theta_S$ and $\theta_{rmw} = \theta_{rmd} = 0$. The relations between the specific wetting parameters m_{mw}, n_{mw} and h_{gmw} and the drying parameters m_{md}, n_{md} and h_{gmd} are unknown at first but it should be kept in mind that the MWC should not cross the MDC.

According to [21] the differential Eq. (3.4) of Parlange does not permit direct calculation of a main wetting curve following the van Genuchten form (instead Parlange used the Brooks and Corey water retention function [12] to obtain the curve illustrated in Fig. 7 left). However, in [21] appropriate conditions are derived for a van Genuchten main wetting curve which approximates the solution of the differential equation. To provide these conditions first the area under the water retention curve is chosen since it is directly related to the work done in wetting or drying the soil. Integration of (3.4) gives

$$(3.7) \quad \begin{aligned} \int \theta_{pd}(h) dh &= \int \theta_{mw}(h) dh - \int (h - h_{stpd}) d\theta_{mw} + c \\ &= 2 \int \theta_{mw}(h) dh - [h - h_{stpd}] \theta_{mw} + c, \end{aligned}$$

where c is a constant of integration, h_{stpd} is the soil water pressure head value on the main wetting curve at which the primary drying curve departs and pd denotes the primary drying curve. When $h_{stpd} = 0$, then θ equals θ_S and the primary drying curve becomes the main drying curve. Combining Eqs. (3.6) and (3.7)₂ results in

$$(3.8) \quad \theta_S \int_0^h \left[1 + \left(\frac{\bar{h}}{h_{gmd}} \right)^{n_{md}} \right]^{-m_{md}} d\bar{h} \\ = 2\theta_S \int_0^h \left[1 + \left(\frac{\bar{h}}{h_{gmw}} \right)^{n_{mw}} \right]^{-m_{mw}} d\bar{h} - \theta_S h \left[1 + \left(\frac{\bar{h}}{h_{gmw}} \right)^{n_{mw}} \right]^{-m_{mw}}.$$

Obviously, for large $\frac{h}{h_{gmw}}$ or $\frac{h}{h_{gmd}}$ the van Genuchten functions (3.6) behave as a power function with exponent $-m_{mw}n_{mw}$ or $-m_{md}n_{md}$. On integrating in (3.8) an exponent $1 - m_{mw}n_{mw}$ or $1 - m_{md}n_{md}$ is obtained. Hence, unless the product $m_{mw}n_{mw} > 1$ (or $m_{md}n_{md} > 1$) the area under the curve becomes infinite. Since, as mentioned above, for the majority of soils, $0 < m_{mw}n_{mw} \leq 1$ (or $0 < m_{md}n_{md} \leq 1$), HAVERKAMP *et al.* sought for conditions canceling the terms in h . Therefore, for $0 < m_{mw}n_{mw} \leq 1$ and/or $0 < m_{md}n_{md} \leq 1$ each term of (3.8) is expanded about $\frac{1}{h} = 0$ as follows

$$(3.9) \quad \left[1 + \left(\frac{h}{h_{gmd}} \right)^{n_{md}} \right]^{-m_{md}} = \left(\frac{h_{gmd}}{h} \right)^{m_{md}n_{md}} - m_{md} \left(\frac{h_{gmd}}{h} \right)^{(1+m_{md})n_{md}} + \dots$$

Integrating and retaining only the leading terms, (3.8) becomes

$$(3.10) \quad \frac{h_{gmd}}{1 - m_{md}n_{md}} \left(\frac{h_{gmd}}{h} \right)^{m_{md}n_{md}-1} \\ = \frac{h_{gmw}}{1 - m_{mw}n_{mw}} \left(\frac{h_{gmw}}{h} \right)^{m_{mw}n_{mw}-1} - h_{gmw} \left(\frac{h_{gmw}}{h} \right)^{m_{mw}n_{mw}-1} + \dots$$

In order to satisfy Eq. (3.10) two conditions are required, namely

$$(3.11) \quad m_{mw}n_{mw} = m_{md}n_{md} \quad \text{and} \quad h_{gmd} = h_{gmw} (1 + m_{mw}n_{mw})^{\frac{1}{m_{mw}n_{mw}}}.$$

Together with (3.3) it follows from (3.11)₁ that

$$(3.12) \quad m_{mw} = m_{md} \quad \text{and} \quad n_{mw} = n_{md}.$$

For $m_{mw}n_{mw} \geq 1$ and/or $m_{md}n_{md} \geq 1$ it has been shown in [21] that (3.11)₂ simplifies to

$$(3.13) \quad h_{gmd} = 2h_{gmw} \quad \text{for} \quad \begin{cases} m_{mw}n_{mw} \geq 1, \\ m_{md}n_{md} \geq 1. \end{cases}$$

The above described procedure and, moreover, the prediction of the primary wetting curve (PWC) from measured data has been demonstrated in [21] for 22 different soil samples. The soil textures range from sands to clayey loams. For each type the MDC has been fitted to experimental data, the MWC and PWC have been predicted theoretically and the latter curve been compared to measured data. In Fig. 8 one example (Del Monte sand, originally presented in [27]) is picked and the measured data of the MDC, the fitted MDC and the predicted MWC are reproduced. The resulting curves are used in the next section to calculate the wave speeds and attenuations of the four waves occurring in partially saturated soils. The range of the acoustic properties is determined in calculating them for the limit cases: once the MDC, the other time the MWC is used as the relation between capillary pressure and saturation.

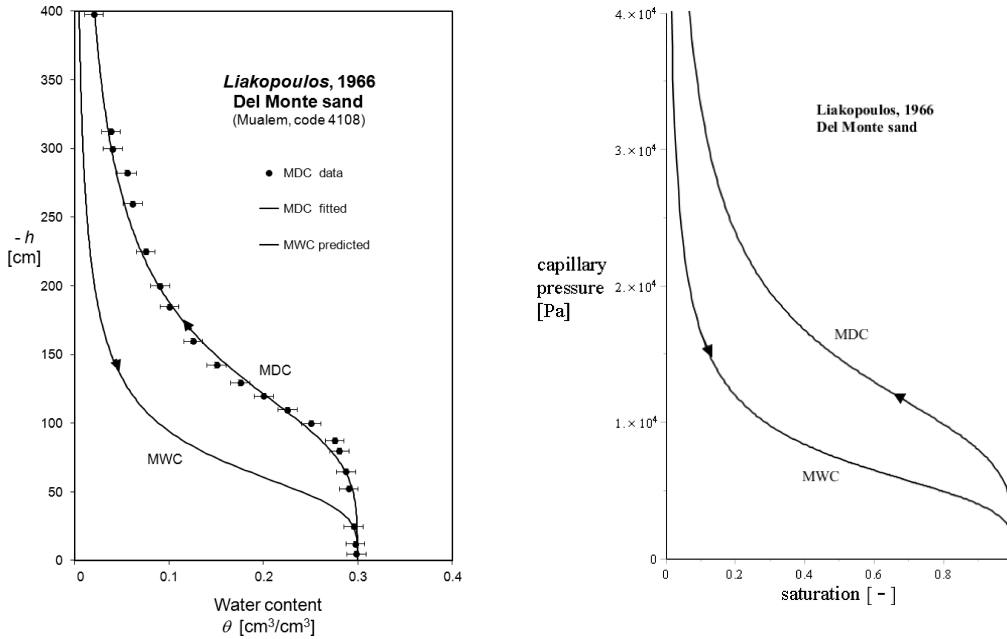


FIG. 8. Left: Main drying curve (MDC) fitted to measured drying data (●) for Del Monte sand taken from Liakopoulos 1966 [27]. The main wetting curve (MWC) has been predicted according to the procedure presented in Subsec. 3.2. Example taken from [21]; right: MDC and MWC for Del Monte sand transformed into capillary pressure-saturation relationship.

4. INFLUENCE ON WAVE PROPAGATION

In the example of Del Monte sand filled by an air-water mixture the influence of the hysteresis in the capillary pressure curve on the propagation of sound waves is studied. This soil type has been chosen because the van Genuchten parameters needed for the prediction of the MWC from the MDC have been already determined in [21] and further material parameters necessary for the calculation of the acoustic properties have been specified in the literature before (e.g. [26]). The material properties of Del Monte sand filled by an air-water mixture are summarized in Table 1. Interestingly, this sand does not possess the above mentioned property that the water retention shape indicator, the product mn , is less than one. In the present case $mn = 2.15$. Since the irreducible saturation is very small nearly the whole range of saturations $0.01 \leq S_0 \leq 1$ has been studied. By specifying the porosity of Del Monte sand by $n_0 = 0.2975$ in

Table 1. Material properties of Del Monte sand filled by an air-water mixture.

real compressibility grains	$K_s = 35 \text{ GPa}$
real compressibility fluid	$K_f = 2.25 \text{ GPa}$
real compressibility gas	$K_s = 0.101 \text{ MPa}$
Poisson's ratio	$\nu = 0.4$
shear modulus	$\mu^S = 0.85 \text{ GPa}$
solid grain density	$\rho^{SR} = 2000 \text{ kg m}^{-3}$
fluid density	$\rho^{FR} = 1000 \text{ kg m}^{-3}$
initial porosity	$n_0 = 0.2975$
intrinsic permeability	$k = 4.5 \cdot 10^{-13} \text{ m}^2$
water conductivity	$K = k \frac{\rho^{FR} g}{\mu_w} = 4.44 \cdot 10^{-6} \text{ m/s}$
water resistance	$\pi^F = \frac{n_0 \rho^{FR} g}{K} = 6.573 \cdot 10^8 \text{ kg m}^{-3} \text{ s}^{-1}$
air resistance	$\pi^G = 1.82 \cdot 10^5 \text{ kg m}^{-3} \text{ s}^{-1}$
water viscosity	$\mu_w = 1 \cdot 10^{-3} \text{ Pa s}$
air viscosity	$\mu_a = 1.82 \cdot 10^{-5} \text{ Pa s}$
van Genuchten parameter	$n = 4.150$
	$m = 0.518$
h_g for drying and wetting	$h_{gd} = 116.56 \text{ cm}$
	$h_{gw} = 58.28 \text{ cm}$
α for drying and wetting	$\alpha_d = 8.745 \cdot 10^{-5} \text{ Pa}$
	$\alpha_w = 1.749 \cdot 10^{-4} \text{ Pa}$
earth acceleration	$g = 9.81 \text{ m s}^{-2}$
pressure head h [m H ₂ O] =	$\frac{\text{capillary pressure } p_c [\text{Pa}]}{\rho^{FR} [\text{kg m}^{-3}] g [\text{m s}^{-2}]} \Rightarrow 1 \text{ [cm H}_2\text{O]} = 100 \text{ [Pa]}$
$\alpha_{d/w}$ [Pa] =	$\frac{1}{10 g [\text{m s}^{-2}] h_{gd/gw} [\text{cm}]}$

[26] it is referred to measurements of Liakopoulos. Therefore this value is also used here even if in the literature bigger values between 34.5% and 37% are also mentioned [22] which in principle sound more realistic for a sand. Also the Poisson ratio of 0.4 seems rather high and the solid grain density of 2000 kg m^{-3} rather low (compared to pure sand (mS) classified in the German standard DIN 4220 and studied in [6]). The rather low value for the water conductivity follows from the small value for the porosity. The value of the shear modulus has been estimated according to experiences gained on the study of some sands in [6].

4.1. Linear model for three-component materials

The linear model for three-component materials with an immiscible mixture of two pore fluids (F and G) in the voids of a solid material (S) has been introduced e.g. in [6]. The fields $\{\mathbf{v}^S, \mathbf{v}^F, \mathbf{v}^G, \mathbf{e}^S, \varepsilon^F, \varepsilon^G\}$, the velocities of the three components, the macroscopic deformation tensor \mathbf{e}^S and the volume changes of fluid and gas, respectively, satisfy the following field equations

$$\begin{aligned}
 \rho_0^S \frac{\partial \mathbf{v}^S}{\partial t} &= \text{div} \{ \lambda^S e \mathbf{1} + 2\mu^S \mathbf{e}^S + Q^F \varepsilon^F \mathbf{1} + Q^G \varepsilon^G \mathbf{1} \} \\
 &\quad + \pi^{FS} (\mathbf{v}^F - \mathbf{v}^S) + \pi^{GS} (\mathbf{v}^G - \mathbf{v}^S), \\
 \rho_0^F \frac{\partial \mathbf{v}^F}{\partial t} &= \text{grad} \{ \rho_0^F \kappa^F \varepsilon^F + Q^F e + Q^{FG} \varepsilon^G \} - \pi^{FS} (\mathbf{v}^F - \mathbf{v}^S), \\
 \rho_0^G \frac{\partial \mathbf{v}^G}{\partial t} &= \text{grad} \{ \rho_0^G \kappa^G \varepsilon^G + Q^G e + Q^{FG} \varepsilon^F \} - \pi^{GS} (\mathbf{v}^G - \mathbf{v}^S), \\
 \frac{\partial \mathbf{e}^S}{\partial t} &= \text{sym grad } \mathbf{v}^S, \quad \frac{\partial \varepsilon^F}{\partial t} = \text{div } \mathbf{v}^F, \\
 \frac{\partial \varepsilon^G}{\partial t} &= \text{div } \mathbf{v}^G, \quad e \equiv \text{tr } \mathbf{e}^S.
 \end{aligned}
 \tag{4.1}$$

Instead of the partial mass densities of the components, ρ^S, ρ^F, ρ^G , the equations depend on the volume changes of the components $e, \varepsilon^F, \varepsilon^G$ for which hold

$$e = \frac{\rho_0^S - \rho^S}{\rho_0^S}, \quad \varepsilon^F = \frac{\rho_0^F - \rho^F}{\rho_0^F}, \quad \varepsilon^G = \frac{\rho_0^G - \rho^G}{\rho_0^G}.
 \tag{4.2}$$

Quantities with subindex zero are initial values of the corresponding current quantity. Q^F, Q^G and Q^{FG} are coupling parameters between solid-fluid, solid-gas and fluid-gas, respectively. λ^S and μ^S are Lamé parameters. The compressibilities of fluid and gas are denoted by κ^F and κ^G .

In principle, the porosity n is also a field and satisfies its own balance equation. However, if we neglect memory effects, the balance equation can be solved and its consideration is no longer necessary to solve the problem. The current

saturation of the fluid S is not included in the series of fields. Instead, a constitutive law of van Genuchten type will be used for this quantity.

Instead of permeabilities resistances of fluid and gas, π^{FS} and π^{GS} , appear in the model which reflect the resistance of the flow through the channels of the skeleton. These parameters are given by

$$(4.3) \quad \pi^{FS} = \frac{\pi^F}{k_f}, \quad \pi^{GS} = \frac{\pi^G}{k_g}.$$

As obvious from Table 1, π^F and π^G account not only for the permeability of the solid but also for the viscosity of the pore fluid. Furthermore, k_f and k_g are relative permeabilities which depend on the degree of saturation. VAN GENUCHTEN [42] not only proposed a theoretical relationship between the capillary pressure and the saturation, but also formulae for these permeabilities

$$(4.4) \quad k_f = S^{1/2} \left[1 - (1 - S^{1/m})^m \right]^2, \quad k_g = (1 - S)^{1/3} \left(1 - S^{1/m} \right)^{2m}.$$

The material parameters $\{\lambda^S + \frac{2}{3}\mu^S, \kappa^F, \kappa^G, Q^F, Q^G, Q^{FG}\}$ appearing in the Cauchy stress tensors in (4.1) have to be specified according to the material. This is done by applying a transition from the micro- to the macro-scale [7]. Therein the formulation of the capillary pressure proposed by van Genuchten (3.1) is used wherein parameters with index vG coincide with those without index quoted in Table 1. Applying the micro-macro transition both to the MDC and the MWC using the microscopic material parameters given in Table 1 leads to the macroscopic material parameters illustrated in Fig. 9.

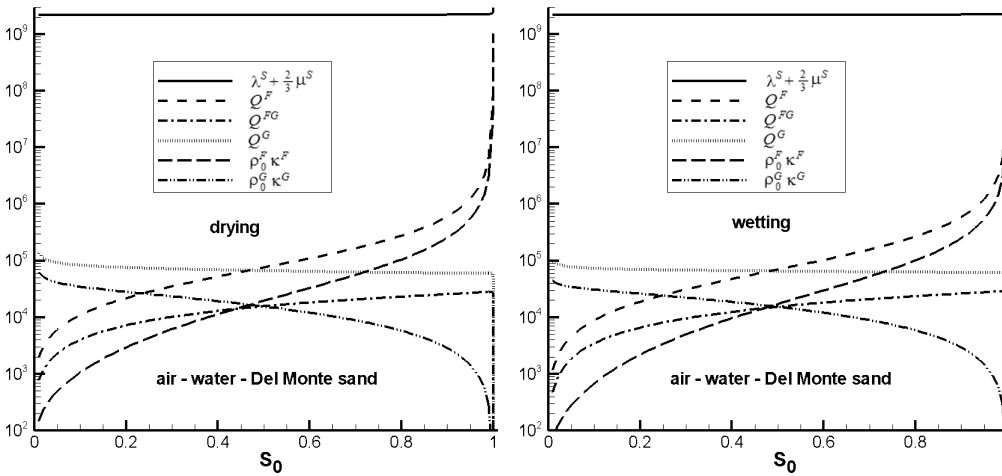


FIG. 9. Macroscopic material parameters appearing in (4.1) in dependence on the initial saturation following from the micro-macro transition procedure introduced in [7]. For the parameters on the left hand side the MDC data, for those on the right hand side the MWC data have been used.

4.2. Propagation of monochromatic waves

The fields of the model (4.1) are assumed to satisfy the following relations

$$(4.5) \quad \begin{aligned} \varepsilon^F &= E^F \mathcal{E}, & \varepsilon^G &= E^G \mathcal{E}, & \mathbf{e}^S &= \mathbf{E}^S \mathcal{E}, \\ \mathbf{v}^F &= \mathbf{V}^F \mathcal{E}, & \mathbf{v}^G &= \mathbf{V}^G \mathcal{E}, & \mathbf{v}^S &= \mathbf{V}^S \mathcal{E}, \\ n - n_0 &= D \mathcal{E}, & \mathcal{E} &:= \exp i(\mathbf{k} \cdot \mathbf{x} - \omega t), \end{aligned}$$

where \mathbf{E}^S , E^F , E^G , \mathbf{V}^S , \mathbf{V}^F , \mathbf{V}^G , D are constant amplitudes, ω is a given frequency, \mathbf{k} is the, possibly complex, wave vector. This means that $\mathbf{k} = k\mathbf{n}$, where k is the complex wave number and \mathbf{n} is a unit vector in the direction of propagation. Such a solution describes the propagation of plane monochromatic waves in an infinite medium whose fronts are perpendicular to \mathbf{n} .

Substitution of the above relations in the field Eqs. (4.1)₄ yields the following compatibility relations

$$(4.6) \quad \begin{aligned} E^F &= -\frac{1}{\omega} k \mathbf{n} \cdot \mathbf{V}^F, & E^G &= -\frac{1}{\omega} k \mathbf{n} \cdot \mathbf{V}^G, \\ \mathbf{E}^S &= -\frac{1}{2\omega} k (\mathbf{n} \otimes \mathbf{V}^S + \mathbf{V}^S \otimes \mathbf{n}), \\ \text{i.e. } e &= -\frac{1}{\omega} k \mathbf{n} \cdot \mathbf{V}^S \mathcal{E}. \end{aligned}$$

Making use of these relations in the remaining field equations leads to the following set

$$(4.7) \quad \begin{aligned} \omega^2 \mathbf{V}^S &= \frac{\lambda^S}{\rho_0^S} k^2 (\mathbf{V}^S \cdot \mathbf{n}) \mathbf{n} + \frac{\mu^S}{\rho_0^S} k^2 ((\mathbf{V}^S \cdot \mathbf{n}) \mathbf{n} + \mathbf{V}^S) + \frac{Q^F}{\rho_0^S} k^2 (\mathbf{V}^F \cdot \mathbf{n}) \mathbf{n} \\ &+ \frac{Q^G}{\rho_0^S} k^2 (\mathbf{V}^G \cdot \mathbf{n}) \mathbf{n} + i \frac{\pi^{FS} \omega}{\rho_0^S} (\mathbf{V}^F - \mathbf{V}^S) + i \frac{\pi^{GS} \omega}{\rho_0^S} (\mathbf{V}^G - \mathbf{V}^S) = 0, \end{aligned}$$

$$(4.8) \quad \begin{aligned} \omega^2 \mathbf{V}^F &= \kappa^F k^2 (\mathbf{V}^F \cdot \mathbf{n}) \mathbf{n} + \frac{Q^F}{\rho_0^F} k^2 (\mathbf{V}^S \cdot \mathbf{n}) \mathbf{n} \\ &+ \frac{Q^{FG}}{\rho_0^F} k^2 (\mathbf{V}^G \cdot \mathbf{n}) \mathbf{n} - i \frac{\pi^{FS} \omega}{\rho_0^F} (\mathbf{V}^F - \mathbf{V}^S) = 0, \end{aligned}$$

$$(4.9) \quad \begin{aligned} \omega^2 \mathbf{V}^G &= \kappa^G k^2 (\mathbf{V}^G \cdot \mathbf{n}) \mathbf{n} + \frac{Q^G}{\rho_0^G} k^2 (\mathbf{V}^S \cdot \mathbf{n}) \mathbf{n} \\ &+ \frac{Q^{FG}}{\rho_0^G} k^2 (\mathbf{V}^F \cdot \mathbf{n}) \mathbf{n} - i \frac{\pi^{GS} \omega}{\rho_0^G} (\mathbf{V}^G - \mathbf{V}^S) = 0. \end{aligned}$$

Separating the contributions and solving the eigenvalue problem yields dispersion relations for transversal and longitudinal waves. Their solutions specify both the phase velocities $c_{ph} = \omega/\text{Re}(k)$ and the attenuations $\text{Im}(k)$. They are illustrated for the MDC and MWC of Del Monte sand filled by an air-water mixture in Figs. 10 to 13. The wave propagation analysis predicts the existence of four sound waves: one transversal wave S and three compressional waves $P1$, $P2$ and $P3$. The $P1$ -wave is mainly driven by the skeleton. The $P2$ -wave shows a similar behavior to the sound wave in suspensions: its speed has a deep minimum in dependence on the saturation. The $P3$ -wave only exists if at least two immiscible pore fluids occur. Its speed is attributed to the capillary pressure between the pore fluids.

The first two figures (Figs. 10 and 11) show the dependence of speeds and attenuations on the frequency ω , the latter two (Figs. 12 and 13) the dependence on the initial saturation.

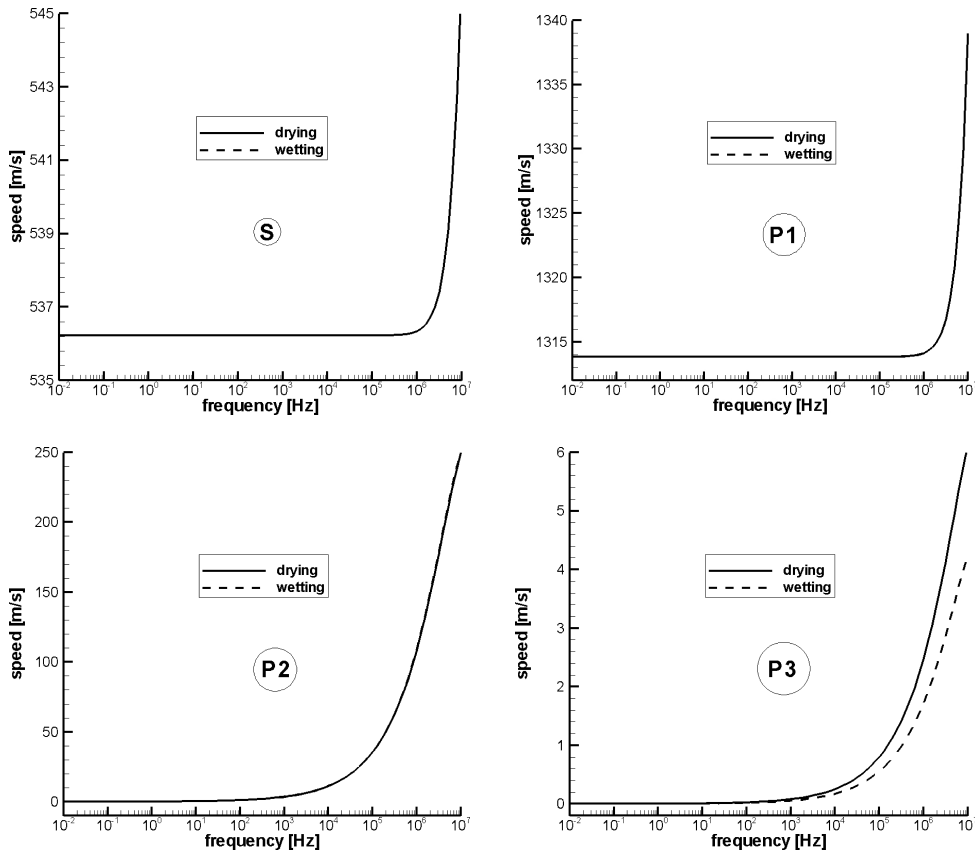


FIG. 10. Phase speeds of the transversal wave S and the three longitudinal waves $P1$, $P2$ and $P3$ in dependence on the frequency ω using the parameters of the MDC (solid lines) and MWC (dashed lines); ($S_0 = 0.8$).

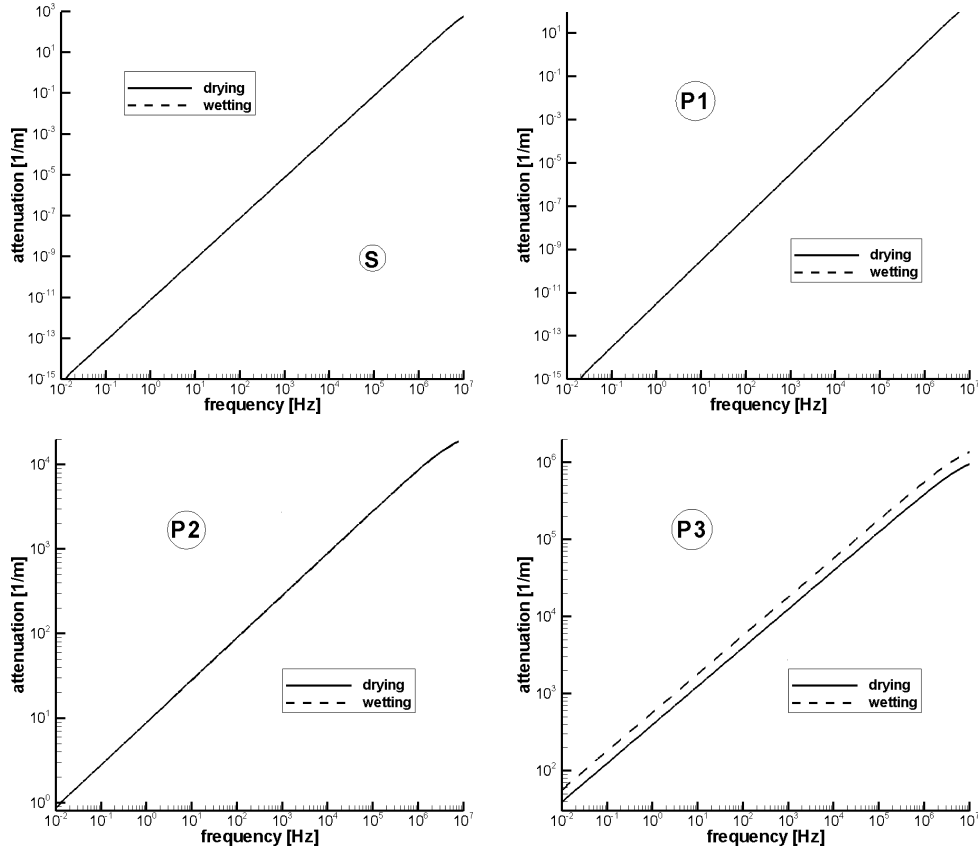


FIG. 11. Attenuations of the transversal wave S and the three longitudinal waves $P1$, $P2$ and $P3$ in dependence on the frequency ω using the parameters of the MDC (solid lines) and MWC (dashed lines); ($S_0 = 0.8$).

4.3. Discussion of results

The results illustrated in Figs. 10 to 13 show that – at least for the example of Del Monte sand filled with an air-water mixture – the influence of the hysteresis is nearly negligible. In the range of frequencies appearing in geophysical applications (around 0 to 1000 Hz) all waves behave almost non-dispersively, i.e. their acoustic properties are nearly unaffected of the frequency. From Figs. 10 and 11 it is obvious that the phase speeds and the attenuations change only for very high values of the frequency. For the waves which are mainly driven by the solid (transversal wave S and the fastest longitudinal wave $P1$) the frequency for which the influence starts lies around 10^6 Hz, for the waves which reflect the properties of the pore fluids ($P2$ and $P3$) it is around 10^3 Hz.

An influence of the application of drying or wetting data is noticeable only for the $P3$ wave. However, this observation most likely does not have any practical

bearing. The $P2$ - and $P3$ -waves, which are effected by the existence of the fluid and the gas, are strongly damped. For the $P3$ -wave the attenuation is so high that an observation of this wave in the field may be nearly impossible. Problems occurred already with the practical observation of the propagation of the $P2$ -wave whose attenuation is high but considerably lower than this of the $P3$ -wave (see Figs. 11 and 13). The $P2$ -wave has been observed for the first time in an artificial porous material made of sintered glass beads by Plona in 1980 [35] and in an artificial rock of cemented sand grains by KLIMENTOS and MCCANN [24] but in situ measurements are extremely difficult to perform. Nevertheless, in 1997 KELDER and SMEULDERS [23] succeeded in the detection of this wave in a sandstone. Attempts to measure the $P3$ -wave are unknown.

From Figs. 12 and 13, which show the dependence of phase speeds and attenuations on the saturation, also for the $P2$ - and $P1$ -wave in the range of low initial saturations (approximately 0–50%) a small influence on wetting or

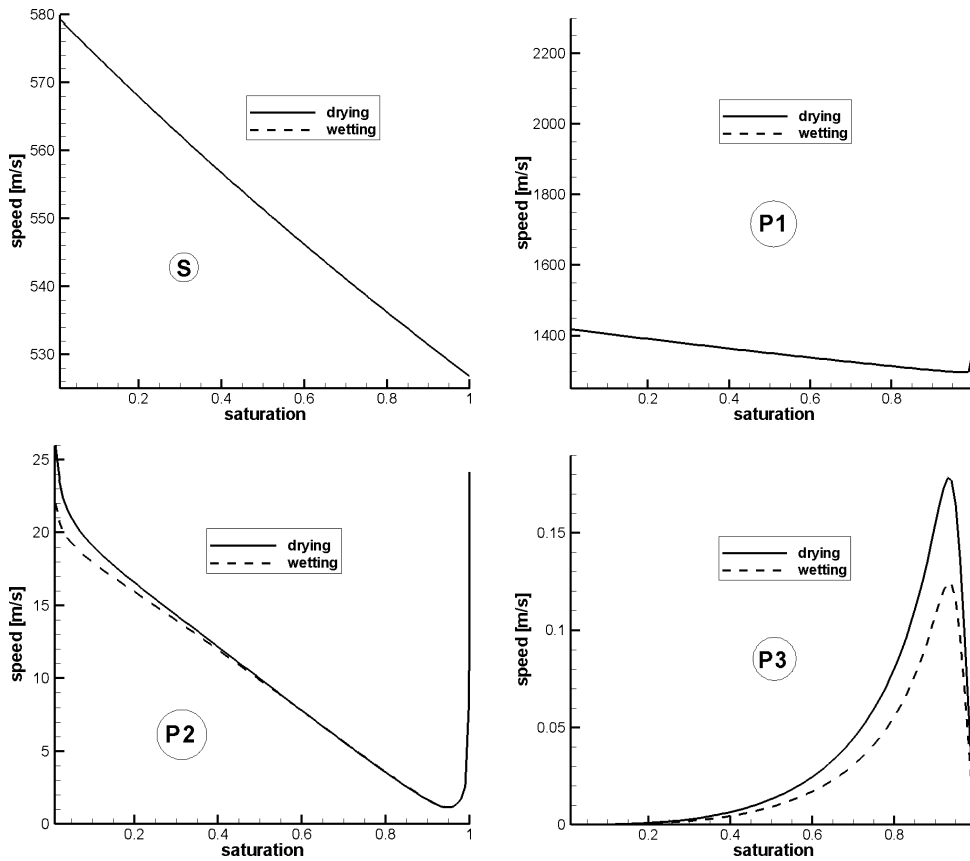


FIG. 12. Phase speeds of the transversal wave S and the three longitudinal waves $P1$, $P2$ and $P3$ in dependence on the initial saturation S_0 using the parameters of the MDC (solid lines) and MWC (dashed lines); ($\omega = 1000$ Hz).

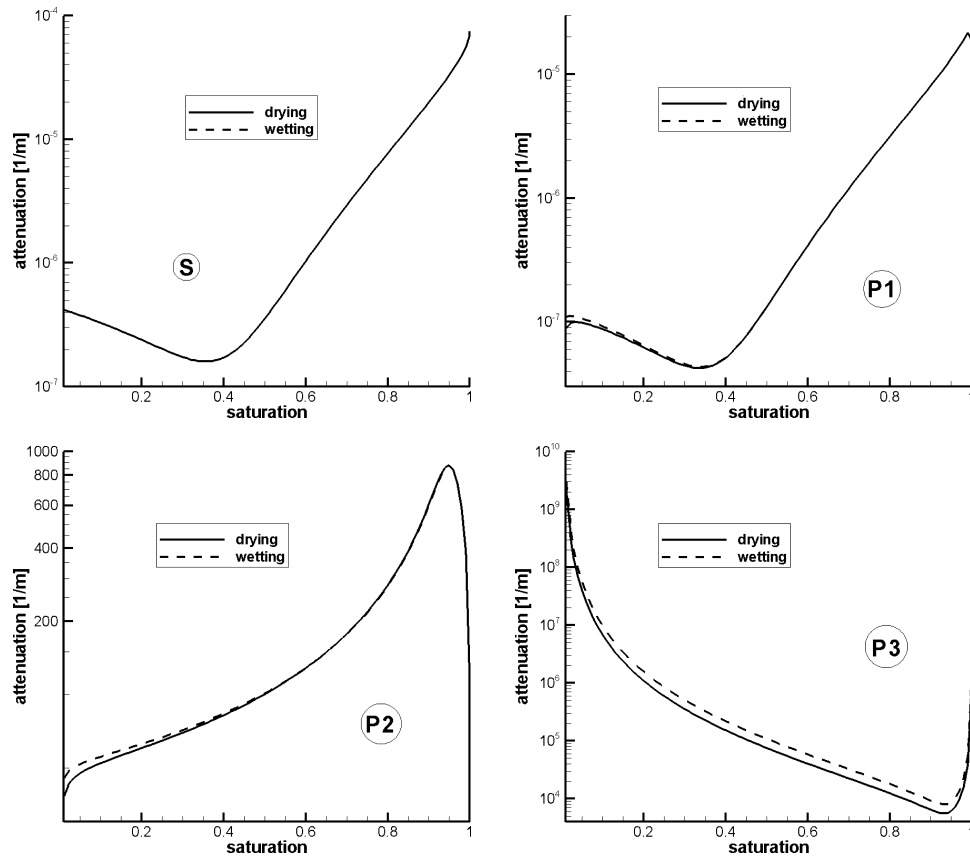


FIG. 13. Attenuations of the transversal wave S and the three longitudinal waves $P1$, $P2$ and $P3$ in dependence on the initial saturation S_0 using the parameters of the MDC (solid lines) and MWC (dashed lines); ($\omega = 1000$ Hz).

drying becomes evident. This is a range of initial saturations which appears in arid regions. It was mentioned above already, that in such regions special measuring techniques are necessary because the capillary pressure or suction is extremely high. Also the theoretical results show that the region of high capillary pressures must be attached an important bearing in the differentiation between wetting and drying. As could be expected, the shear wave which is mainly affected by the shear modulus, the compressibility modulus and the mass density of the solid, is indifferent to whether drying or wetting data are used. In contrast, the propagation of the $P3$ -wave is influenced in the whole range of initial saturations. This could be expected because this wave arises only due to the capillary pressure or surface tension between the two pore fluids and this is different for drying and wetting for different saturations (remember Fig. 8). The big difference in the MDC and MWC even led to the expectation of bigger differences in the acoustic properties of the $P3$ -wave.

5. CONCLUSIONS AND OUTLOOK

In this work the phenomenon of different drying and wetting curves for the capillary pressure in partially saturated soils has been brought up. Measurement methods of the capillary pressure or suction and their ranges of application have been shown. The van Genuchten approach for the description of one branch of the capillary pressure curve has been highlighted. It is used in the prediction method for main drying and main wetting curves (also for further scanning curves which is not covered in this paper) of HAVERKAMP *et al.* which has been used for the investigation of the influence of the application of drying and wetting data on the propagation of sound waves. It has been studied theoretically by means of a linear continuum model presented in [6] and numerically exploited for the example of Del Monte sand filled by an air-water mixture. Four waves appear: one transversal wave and three longitudinal waves. For the waves driven mainly by the skeleton it could be expected that the influence of the hysteresis in the capillary pressure curve is negligible. This is different from the expectations for the pore fluid driven waves. The numerical results exhibit a smaller influence than expected. This may have several reasons: firstly, the porosity of the studied sand has been chosen rather small – in the literature are also higher values reported. Secondly, the soil type definitely has an influence. It may be not sufficient to investigate only one soil type. Thirdly, the prediction of the main wetting curve should be proven by experimental data. In order to clarify whether any of these causes is responsible for the small influence of the hysteresis on the wave properties, measurements of the main drying and wetting curves of the twelve soil types studied in [6] have been requested in a laboratory and will be interpreted theoretically once available. Moreover, the hysteresis phenomenon will be studied mathematically in closed form by use of an hysteresis operator.

ACKNOWLEDGMENT

Financial support as an Einstein Junior Fellow by the Einstein Foundation Berlin is highly appreciated.

REFERENCES

1. <http://archives.sensorsmag.com/articles/0505/30/main.shtml>.
2. http://beesl.syr.edu/ht_1d-sutud-moist-stor.htm.
3. <http://www.soilmeasurement.com/tempe.html>.
4. ALBERS B., *On the influence of saturation and frequency on monochromatic plane waves in unsaturated soils*, [in:] Coupled site and soil-structure interaction effects with application to seismic risk mitigation, T. Schanz and R. Iankov [Eds.], NATO Science Series, Springer Netherlands, pp. 65–76, 2009.

5. ALBERS B., *Micro-macro transition and linear wave propagation in three-component compacted granular materials*, [in:] AIP Conference Proceedings of the Joint IUTAM-ISIMM Symposium on Mathematical Modeling and Physical Instances of Granular Flows, J. Goddard and P. Giovine [Eds.], AIP, 2010.
6. ALBERS B., *Modeling and Numerical Analysis of Wave Propagation in Saturated and Partially Saturated Porous Media*, Veröffentlichungen des Grundbauinstitutes der Technischen Universität Berlin, Habilitation thesis, Shaker Verlag, Aachen, vol. 48, 2010.
7. ALBERS B., *On a micro-macro transition for a poroelastic three-component model*, ZAMM, **90**, 12, 929–943, 2010.
8. ALBERS B., *Linear elastic wave propagation in unsaturated sands, silts, loams and clays*, Transport in Porous Media, **86**, 537–557, 2011.
9. ALBERS B., *Modeling the hysteretic behavior of the capillary pressure in partially saturated porous media – a review*, Acta Mech., **225**, 2163–2189, 2014.
10. ALBRECHT B.A., BENSON C.H., BEUERMANN S., *Polymer capacitance sensors for measuring soil gas humidity in drier soils*, J. Geotechnical Testing, **26**, 1, 1–9, 2003.
11. BEAR J., BACHMAT Y., *Introduction to Modeling of Transport Phenomena in Porous Media*, Kluwer Academic Publishers, Dordrecht, 1991.
12. BROOKS R.H., COREY A.T., *Hydraulic properties of porous media*, [in:] Hydrology Papers, vol. 3, Colorado State University, Fort Collins, 1964.
13. BUCKINGHAM E., *Studies on the Movement of Soil Moisture*, United States Department of Agriculture, Bureau of Soils Bulletin, vol. 38, U. S. Department of Agriculture, 1907.
14. BULUT R., *Total and matric suction measurements with the filter paper method*, <http://www.foundationperformance.org/pastpresentations/FilterPapSuctMeasDemonstrtn.pdf>.
15. CAMPBELL-CLAUDE J.M., *Using gypsum blocks to measure soil moisture in vineyards*, Farmnotes, **3**, 1998.
16. DANE J.H., HOPMANS J.W., *Water retention and storage*, Methods of Soil Analysis, **4**, 671–717, 2002.
17. DIN 4220: *Pedologic site assessment – Designation, classification and deduction of soil parameters (normative and nominal scaling)*, DIN Deutsches Institut für Normung e.V., Beuth Verlag GmbH (draft, in German: *Bodenkundliche Standortbeurteilung – Kennzeichnung, Klassifizierung und Ableitung von Bodenkennwerten (normative und nominale Skalierungen)*), 2005.
18. ENDERBY J.A., *The domain model of hysteresis, Part 1 – independent domains*, Trans. Faraday Soc., **51**, 835–848, 1955.
19. EVERETT D.H., *A general approach to hysteresis. Part 3 – a formal treatment of the independent domain model of hysteresis*, Transactions of the Faraday Society, **50**, 1077–1096, 1954.
20. FREDLUND D.G., RAHARDJO H., *Soil Mechanics for Unsaturated Soils*, John Wiley & Sons, 1993.
21. HAVERKAMP R., REGGIANI P., ROSS P.J., PARLANGE J.-Y., *Soil water hysteresis prediction model based on theory and geometric scaling*, [in:] Environmental Mechanics, Water, Mass and Energy Transfer in the Biosphere, A. W. P.A.C. Raats, D. Smiles [Eds.], American Geophysical Union, pp. 213–246, 2002.
22. JOHNSON A.I., MORRIS D.A., *Vibratory compaction in the laboratory of granular materials in long columns*, [in:] Evaluation of relative density and its role in geotechnical projects involving cohesionless soils: a symposium presented at the 75th annual meeting, ASTM STP 523, American Society for Testing and Materials, 1973.

23. KELDER O., SMEULDERS D.M.J., *Observation of the Biot slow wave in water-saturated Nivelsteiner sandstone*, Geophysics, **62**, 6, 1794–1796, 1997.
24. KLIMENTOS T., MCCANN C., *Why is the Biot slow compressional wave not observed in real rocks?*, Geophysics, **53**, 12, 1605–1609, 1988.
25. KOOL J.B., PARKER J.C., *Development and evaluation of closed-form expressions for hysteretic soil hydraulic properties*, Water Resources Research, **23**, 1, 105–114, 1987.
26. LEWIS R.W., SCHREFLER B.A., *The finite element method in the static and dynamic deformation and consolidation of porous media*, Wiley, Chichester, 1998.
27. LIAKOPOULOS A.C., *Theoretical approach to the solution of the infiltration problem*, International Association of Scientific Hydrology, Bulletin, **11**, 1, 69–110, 1966.
28. LINS Y., *Hydro-mechanical properties of partially saturated sand*, PhD Thesis, Schriftenreihe des Lehrstuhls für Grundbau, Boden- und Felsmechanik, vol. 42, Ruhr-Universität Bochum, 2010.
29. LU N., LIKOS W., *Unsaturated Soil Mechanics*, Wiley, Hoboken, New Jersey, 2004.
30. MUALEM Y., *A conceptual model of hysteresis*, Water Resources Research, **10**, 514–520, 1974.
31. MUALEM Y., *A new model predicting the hydraulic conductivity of unsaturated porous media*, Water Resour. Res., **12**, 513–522, 1976.
32. NÉEL L., *Théories des lois d'aimantation de Lord Rayleigh, I: Les déplacements d'une paroi isolée*, Cahiers de Physique, **12**, 1, 1–20, 1942.
33. PARKER J.C., LENHARD R.J., *A model for hysteretic constitutive relations governing multiphase flow, 1. saturation-pressure relations*, Water Resources Research, **23**, 12, 2187–2196, 1987.
34. PARLANGE J.-Y., *Capillary hysteresis and the relationship between drying and wetting curves*, Water Resources Research, **12**, 2, 224–228, 1976.
35. PLONA T.J., *Observation of a second bulk compressional wave in a porous medium at ultrasonic frequencies*, Appl. Phys. Lett., **36**, 4, 259–261, 1980.
36. POULOVASSILLIS A., *Hysteresis of pore water in granular porous bodies*, Soil Science, **109**, 1, 5–12, 1970.
37. REINSON J.R., FREDLUND D.G., WILSON G.W., *Unsaturated flow in coarse porous media*, Can. Geotech. J., **42**, 252–262, 2005.
38. SCHANZ T., MIKULITSCH V., LINS Y., *Untersuchungen an teilgesättigten, granularen reibungsmaterialien*, [in:] 3. Workshop – Teilgesättigte Böden (Bauhaus-Universität Weimar), pp. 145–159, 2001.
39. SCOTT P.S., FARQUHAR G.J., KOUWEN N., *Hysteretic effects on net infiltration*, [in:] Advances in Infiltration, pp. 163–171, 1983.
40. SHETA H., *Simulation von Mehrphasenvorgängen in porösen Medien unter Einbeziehung von Hysterese-Effekten* [in German], PhD Thesis, Universität Stuttgart, 1999.
41. TOPP G.C., *Soil water hysteresis in silt loam and clay loam soils*, Water Resources Research, **7**, 4, 914–920, 1971.
42. VAN GENUCHTEN M.T., *A closed-form equation for predicting the hydraulic conductivity of unsaturated soils*, Soil Sci. Soc. Am. J., **44**, 892–898, 1980.